Journal of ELECTRONIC MATERIALS, Vol. 41, No. 5, 2012
DOI: 10.1007/s11664-012-2094-6

MOCVD Growth of Erbium Monoantimonide Thin Film and Nanocomposites for Thermoelectrics

KATE J. NORRIS,[1,2,3,5] ANDREW J. LOHN,[1,2,3] TAKEHIRO ONISHI,[1] ELANE COLEMAN,[4] VERNON WONG,[1,2,3] ALI SHAKOURI,[1] GARY S. TOMPA,[4] and NOBUHIKO P. KOBAYASHI[1,2,3]

1.—Baskin School of Engineering, University of California, Santa Cruz, Santa Cruz, CA 95064, USA. 2.—Nanostructured Energy Conversion Technology and Research (NECTAR), Advanced Studies Laboratories (ASL), University of California Santa Cruz, Santa Cruz, CA 95064, USA. 3.—NASA Ames Research Center, Moffett Field, CA 94035, USA. 4.—Structured Materials Industries Inc., Unit 102/103, 201 Circle Drive North, Piscataway, NJ 08854, USA. 5.—e-mail: katejeannenorris@gmail.com

We report the growth of erbium monoantimonide (ErSb) thin films on indium antimonide (100) substrates by low-pressure metalorganic chemical vapor deposition. The growth rate of ErSb thin films shows strong dependency on the growth temperature and the Sb/Er precursor molar flow rate ratio. Scanning electron microscopy, energy-dispersive x-ray spectroscopy, and x-ray diffractometry (XRD) were employed to study the ErSb thin films grown under the growth conditions that gave the maximum growth rate in the range we investigated. We also report the growth of two types of nanocomposites in which ErSb nanocolumns or nanoslabs with lengths ~500 nm and diameters 20 nm to 30 nm are embedded in Zn-doped InGaSb (ErSb/InGaSb:Zn) and ErSb nanoparticles with diameters of ~30 nm are embedded in Zn-doped InSbAs (ErSb/InSbAs:Zn). These nanocomposites were intended to increase phonon scattering in a mid-to-long phonon wavelength range to reduce lattice thermal conductivity. We used time-domain thermoreflectance to measure total thermal conductivity for the two types of nanocomposites, obtaining 4.0 ± 0.6 W/mK and 6.7 ± 0.8 W/mK for the ErSb/InAsSb:Zn and ErSb/InGaSb:Zn nanocomposites, respectively, which suggests that the thermal conductivity was close to or slightly smaller than the alloy limit of the two ternary alloy hosts. The two nanocomposites were further studied by transmission electron microscopy (TEM) to reveal their microscopic features and by XRD to assess their crystalline structures.

Key words: InGaSb, InSbAs, MOCVD, ErSb, Thermoelectric, Thermal conductivity

INTRODUCTION

Demand for green energy has spurred the search for carbon-free energy sources by harvesting waste energy. Thermoelectrics are environmentally friendly power sources under growing investigation that convert a temperature gradient into electric power. The standard guideline in the search for efficient thermoelectric materials for low-temperature applications is to identify narrow-band-gap semiconductors with high carrier mobility.[1] The efficiency of a thermoelectric material is a function of the dimensionless figure of merit ZT, where $ZT = S^2\sigma T/\kappa$; S is the Seebeck coefficient, σ is the electrical conductivity, T is absolute temperature, and κ is the thermal conductivity.[2] The value $ZT \approx 1$ for bismuth telluride, BiTe, alloys near room temperature discovered in the 1950s is necessary for practical applications. However, due to the interdependence of the components of the

(Received August 16, 2011; accepted March 28, 2012; published online April 24, 2012)

dimensionless figure of merit, it has been difficult to achieve $ZT > 1$.[3] To improve ZT, one can increase the power factor, $S^2\sigma$, and/or reduce the thermal conductivity, κ. There are various approaches to achieve higher ZT, such as introducing peaks in the density of states,[4] phonon scattering by "guest atoms,"[5] one-dimensional nanostructures,[3] and superlattices.[6] A record high ZT of 2.65 and a thermal conductivity of 0.031 W/mK were measured for a Bi_2Te_3 single thin layer prepared by laser ablation.[7] Additionally, a ZT of ~2.4 has been reported for a Bi_2Te_3/Sb_2Te_3 superlattice by Venkatasubramanian.[6]

We focused on reducing thermal conductivity. Thermal conductivity, κ, is broken down into the contributions from lattice vibrations (i.e., phonons) and from charged carriers. The lattice contribution can be suppressed by using the concept of "nanocomposites," i.e., semimetallic nanoparticles embedded in an alloy host semiconductor. Recent advances utilizing ErAs semimetallic nanoparticles embedded in an alloy host semiconductor made of one of the group III–V compound semiconductors have shown that the lattice thermal conductivity can be reduced to near its theoretical limit.[8–11] Much remains to be explored in the understanding of phonon transport in nanostructured materials despite attempts in this regard.[12]

To further enhance the thermoelectric properties of nanocomposites we designed nanocomposites with ErSb nanostructures embedded in two types of alloy host semiconductors: $In_xGa_{1-x}Sb$ and $InSb_{1-y}As_y$. Embedded semimetallic nanoparticles, for instance, can maintain electrical properties and optimize heat transport properties of the host semiconductors by working as mid- to long-wavelength phonon scattering sources,[13,14] along with dopants.[15] The thermoelectric power factor ($S^2\sigma$) is also enhanced by nanoparticles.[9] It was also reported that ZT increased with reduction in embedded nanoparticle size.[8]

While ErSb has been grown exclusively by molecular beam epitaxy,[9,16,17] we demonstrated growth of ErSb by metalorganic chemical vapor deposition (MOCVD) on InSb(100) substrates. In our demonstration, ErSb was deposited in the form of either thin films or nanostructures in a host semiconductor as mentioned earlier. Two types of ErSb nanostructures have been identified: nanoparticles and nanocolumns embedded in a host ($In_{1-x}Ga_xSb$ or $InSb_{1-y}As_y$) ternary alloy. Our research has demonstrated the potential of nanocomposites to reduce thermal conductivity below the alloy limit, practically improving ZT and providing a method to grow ErSb-based nanocomposites by MOCVD for a wide range of viable applications.

EXPERIMENTAL PROCEDURES

ErSb Thin Films on InSb(100) Substrates

Low-pressure MOCVD was used to grow ErSb thin films on epiready InSb(100) substrates. An InSb(100) substrate was placed on a susceptor held in a reaction chamber made of quartz. The surface of InSb(100) substrate was thermally deoxidized before the deposition of an InSb buffer layer and a subsequent ErSb thin film. The precursors, triethylantimony (TESb) and tris-isopropylcyclopentadienyl erbium (iPrCp 3Er), were carried by purified hydrogen gas to the reaction chamber. The growth temperature, pressure, and molar flow rates were 485°C, 180 Torr, and 5.58×10^{-5} mol/min of TESb and 1.37×10^{-5} mol/min of iPrCp 3Er, respectively. The growth was performed with plasma-assisted deposition.

Figure 1 shows the deposition rate of ErSb thin films on InSb(100). As clearly shown in Fig. 1, the growth rate of an ErSb thin film was found to be strongly dependent on both the growth temperature and the Er/Sb precursor flow rate ratio. Figure 1 indicates a sharp peak of 0.0833 nm/s at substrate temperature of 485°C and precursor V/III molar flow rate ratio of 2.25. An interesting feature is that the deposition rate falls off more slowly at lower precursor flow rates and higher growth temperatures, while reducing more quickly at higher flow rates. The incorporation of Er on initial InSb surfaces in the high-temperature regime in Fig. 1 may have been reduced by significant preferential desorption of Sb from InSb, expected at temperatures close to the melting temperature of InSb (527°C). In addition, the growth rate is most likely suppressed at lower precursor ratios because of Sb deficiency. Once formed, the ErSb should be thermally stable within the growth temperatures investigated in Fig. 1, as the melting temperature of ErSb is above 2000°C.

Nanocomposite: ErSb Nanostructures Embedded in a Ternary Alloy Host

After completing the calibration of ErSb thin-film growth, we conducted epitaxial growth of nanocomposites in which ErSb nanostructures were embedded in either Zn-doped InGaSb or Zn-doped InSbAs host grown on InSb(100) substrates by

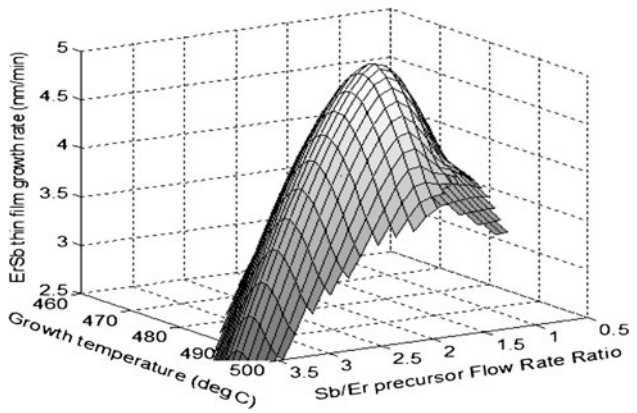

Fig. 1. ErSb thin-film deposition rate on InSb(100) substrates.

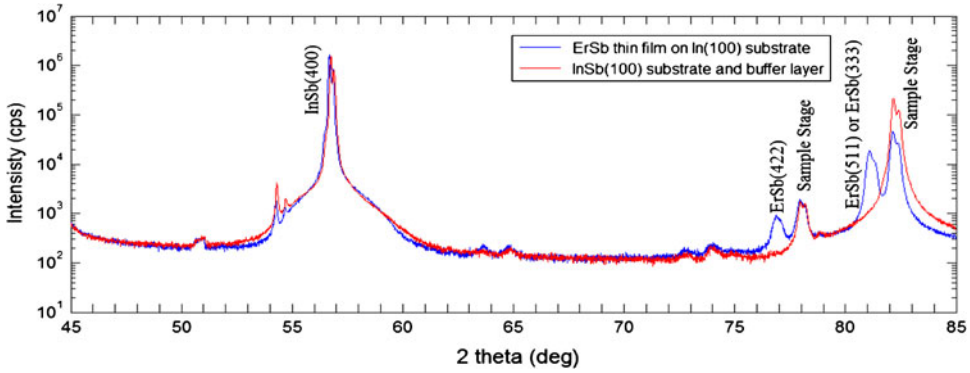

Fig. 2. XRD profile of an ErSb thin film grown on an InSb buffer layer on an InSb(100) substrate compared with that of an InSb(100) substrate.

low-pressure MOCVD. For both hosts, MOCVD growths were conducted at substrate temperature of 485°C and reactor pressure of 200 Torr. The precursors trimethylindium (TMIn), TESb, and triethylgallium (TEGa) were used for the InGaSb:Zn host with molar flow rate ratio of 1.05:1.49:0.92, respectively. The precursors for the InSbAs:Zn host were TMIn, TESb, and triethylarsine (TEAs) with molar flow rate ratio of 1.05:1.49:0.89. Diethylzinc (DEZn) was flowed at 1.93×10^{-6} mol/min for both host materials. For both host materials, the erbium precursor, iPrCp 3Er, was injected into the reaction chamber at 1.70×10^{-4} mol/min.

RESULTS AND DISCUSSION

ErSb Thin Films on InSb(100) Substrates

Even at the highest growth rate, the grown ErSb thin films showed smooth surface morphology. Energy-dispersive x-ray spectroscopy (not shown) confirmed that both Er and Sb were present in the thin films as well as the In and Sb from the substrate. The XRD profiles collected from the ErSb thin film grown on an InSb(100) substrate are shown in Fig. 2. Based on multiple diffraction peaks from the InSb(100) substrate and InSb buffer layers, the buffer layers are likely to be polycrystalline, being at best highly oriented textured films. As indicated in Fig. 2, we were unable to index some peaks, although these unidentified peaks did not impact on relevant analyses. Two distinct peaks indexed to ErSb(422) and ErSb(511) or ErSb(333) indicate that the ErSb thin film has two preferential growth orientations over [100] direction expected for simple epitaxial growth on InSb(100) substrates. This suggests that the grown ErSb thin film has crystallographic registration rotated and/or tilted with respect to the substrate, as previously reported by Palmstrøm et al.[18] The polycrystalline nature of the buffer layer could also explain why ErSb takes on these unusual orientations.

To further investigate the microscopic crystal structure of the ErSb thin film, we referred to the structure factor of the rock-salt crystal structure to obtain $F(422) = 280$ and $F(511) = 34$;[19,20] therefore, the intensity of the ErSb(422) peak should have been $(280/34)^2 = 67.8$ times stronger than the ErSb(511) peak if two types of crystallites having these two planes as preferential orientations had the same volume fraction. In Fig. 2, we obtained the ratio of the two diffraction peak intensities as $I(511)/I(422) = 16{,}670/826 = 20.18$, then we calculated the ratio of the number of unit cells that would result in the obtained ratio of the diffraction peak intensities as $N(511)/N(422) \approx 37$.[19] Therefore, the grown ErSb thin film has volume ratio of approximately 97.4% ErSb(511) majority orientation and 2.6% ErSb(422). These results indicate that, in an ErSb thin film grown on an InSb(100) substrate, ErSb(511) oriented phases dominate, with a small fraction of ErSb(422) phases. In contrast, peaks associated with ErSb(n00) families did not appear in Fig. 2, suggesting that the grown ErSb thin film does not have a crystallographic registration typically expected from epitaxial thin films.

Nanocomposite: ErSb Nanostructures Embedded in a Ternary Alloy Host

The XRD profiles in Figs. 3 and 4 were collected from two types of nanocomposites: ErSb/InGaSb:Zn nanocomposite and ErSb/InSbAs:Zn nanocomposite, respectively. Embedded ErSb nanostructures did not appear in the XRD profiles, presumably because the volume of each nanostructure spatially isolated from others is too small to cause sharp, intense diffraction peaks. While the grown InSb buffer layer is likely polycrystalline based on the XRD profile in Fig. 2, it is possible that a selection process of a dominant crystallographic orientation can induce epitaxial growth of a subsequent layer during the growth of the InGaAs/ErSb and InAsSb/ErSb nanocomposites.[21] From the (004) and (002) peak shifts in Figs. 3 and 4, alloy compositions were obtained for the $In_{1-x}Ga_xSb$:Zn ($x = 0.975$) and the $InSb_{1-y}As_y$:Zn ($y = 0.406$). There is a possible compositional variation in the InGaSb host material that would be overlaid onto the contrast created by the host and embedded ErSb.

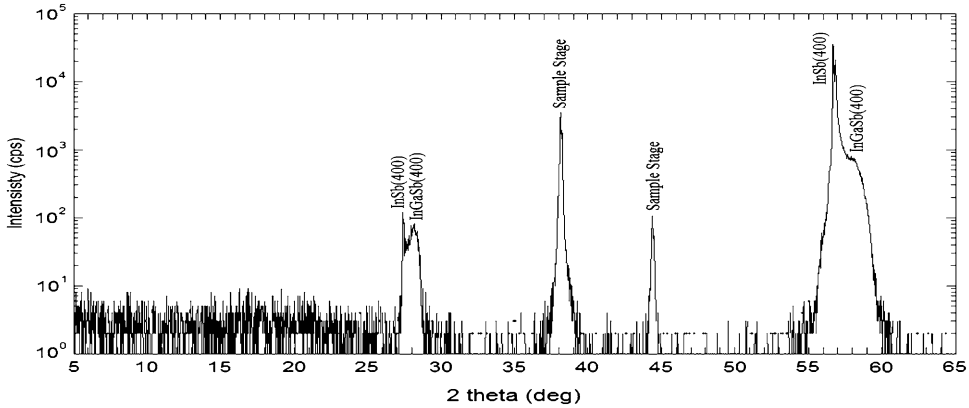

Fig. 3. XRD profile of the ErSb/$In_{1-x}Ga_xSb$:Zn (x = 0.975) nanocomposite.

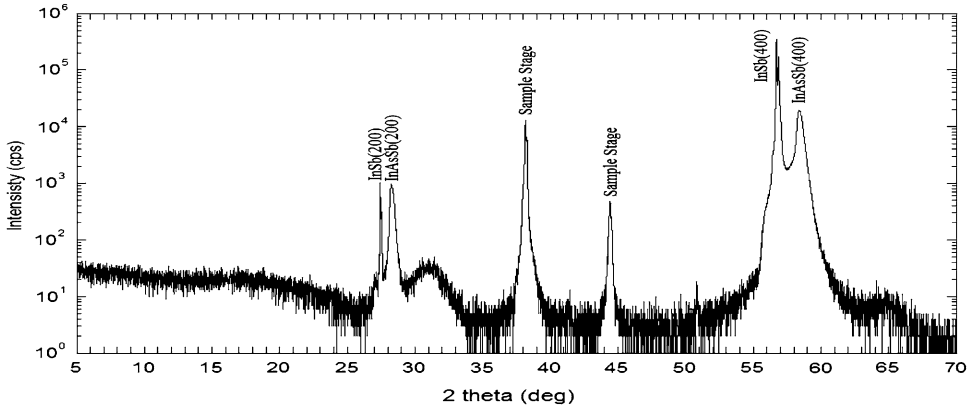

Fig. 4. XRD profile of the ErSb/$InSb_{1-y}As_y$:Zn (y = 0.406) nanocomposite.

Cross-sectional TEM was used to analyze the structural characteristics of the two types of nanocomposites (ErSb/InGaSb:Zn and ErSb/InSbAs:Zn) as shown in Figs. 5 and 6, respectively. The TEM images were collected with [110] zone axis. Figure 5 reveals that a group of 20-nm- to 30-nm-diameter ErSb nanocolumns or nanoslabs formed in the InGaSb:Zn host. These nanometer-scale structures seen in Fig. 5 could be "nanoslabs," i.e., long-range periodical structures such as ErSb/InGaSb lateral superlattice, or nanocolumns, or nanocolumns. However, the nanocolumn arrangement has been reported elsewhere.[22] Most of the nanocolumns appear to be parallel to each other. This would indicate that the ErSb nanocomposites grew preferentially in the InSb(100) substrate's crystallographic orientation. Figure 6 shows a large number of ~30-nm-diameter ErSb nanoparticles formed in the InAsSb:Zn host. The nanoparticles appear to be distributed throughout the sample. The formation of ErSb nanoparticles is likely to be spontaneous.[8] Higher concentrations of erbium along with a relatively high erbium diffusion rate on the surface could have allowed larger ErSb nanoparticles to gradually grow into ErSb nanocolumns.[22]

As described earlier, one of the key thermoelectric characteristics that directly influence ZT is the thermal conductivity of a material. We used time-domain thermoreflectance (TDTR)[23] to determine the thermal conductivity of the two types of nanocomposites at room temperature. TDTR measurements provide total thermal conductivity (i.e., the sum of the lattice and the electronic contributions to thermal conductivity). Surface roughness on the Al layers affects the TDTR results through the variation in the Al layer thickness. The Al layers were measured with an acoustic echo in the TDTR measurement. This systematic error is estimated to be ±5%, reflecting the variation in the Al thickness. Other sources of error include the uncertainties of the laser beam size and the heat capacities of the layers. The thermal conductivity obtained for the ErSb/InSbAs:Zn at room temperature was 4.0 ± 0.6 W/mK. This is slightly lower than the value of ~5 W/mK obtained for the InSbAs alloy limit at the composition we experimentally examined.[24] We also determined the thermal conductivity of the ErSb/InGaSb:Zn at room temperature to be 6.7 ± 0.8 W/mK, which is slightly higher than the alloy limit of ~5 W/mK.[25] We would have seen observable reduction in the lattice contribution, as theory

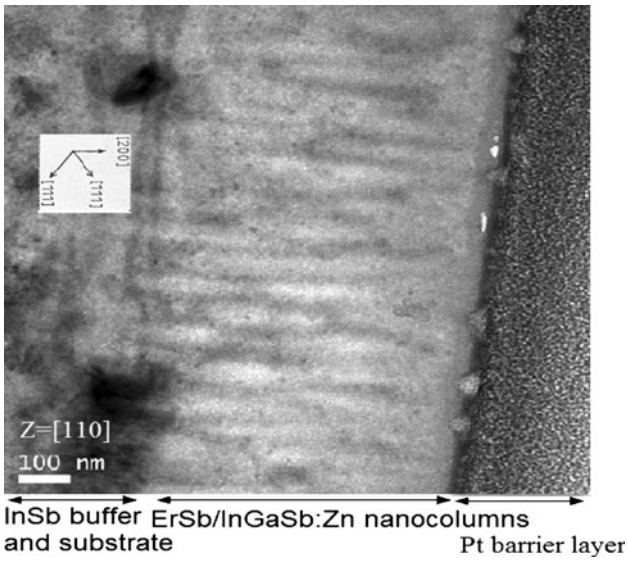

Fig. 5. TEM image of the ErSb/InGaSb:Zn nanocomposite showing a group of 20-nm- to 30-nm-diameter nanocolumns or nanoslabs.

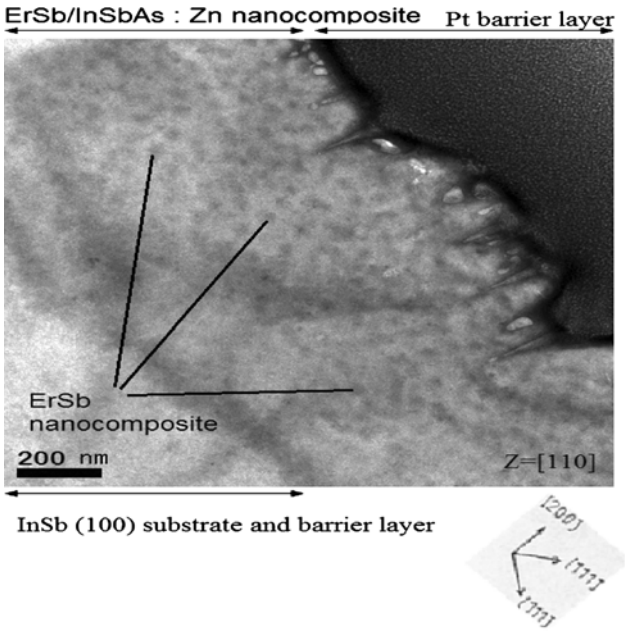

Fig. 6. TEM image of the ErSb/InSbAs:Zn showing a large number of 20-nm- to 35-nm-diameter nanoparticles.

predicts the nanocomposites to behave as mid- to long-wavelength phonon scattering sources[13,14] if the size of the embedded ErSb nanostructures were appropriately tuned.

CONCLUSIONS

We demonstrated MOCVD growth of ErSb thin films on InSb(100) substrates. While EDX analysis confirmed that the grown ErSb thin films are made of all expected chemical elements, the XRD profile suggested that ErSb(511) or ErSb(333) phase dominates the thin film. We also demonstrated growth of two types of nanocomposites: ErSb/$In_{1-x}Ga_xSb$:Zn and ErSb/$InSb_{1-y}As_y$:Zn by low-pressure MOCVD. In the InGaSb:Zn host, TEM analysis revealed that ErSb grew as nanopillars with ~500 nm length and 20 nm to 30 nm diameter almost vertical to the substrate, while ErSb nanoparticles with diameter ~30 nm were identified in the InSbAs:Zn host. The measured thermal conductivities of the two types of nanocomposites showed promising results; however, further tuning (e.g., size and volume fraction of ErSb nanostructures) is necessary to validate the concept of nanocomposites within the context of thermoelectric materials, and further investigation is required to address specific growth mechanisms that resulted in the two types of ErSb nanostructures (i.e., nanocolumns/slabs and nanoparticles) depending on the host type.

ACKNOWLEDGMENT

This work was supported by DARPA/DSO, DoE, and ONR. We would like to thank Dr. Jae Hun Seol of UC Berkeley and Dr. Gilles Pernot of UC Santa Cruz for sample preparation and TDTR measurement. The authors are grateful to Dr. Stephan Kraemer, Dr. Hong Lu, and Prof. Art Gossard for the TEM imaging at UC Santa Barbara. The authors would also like to thank Hewlett-Packard Labs (Palo Alto, CA) for their support and use of equipment.

REFERENCES

1. I. Terasaki, Y. Sasago, and K. Uchinokura. (1997) doi: 10.1103/PhysRevB.56.R12685.
2. G. Chen, T. Caillat, M.S. Dresselhaus, G. Dresselhaus, and J.P. Fleurial (2003) doi:10.1179/095066003225010182.
3. C.J. Vineis, A. Shakouri, A. Majumdar, and M.G. Kanatzidis (2010) doi:10.1002/adma.201000839.
4. J. Lee, J. Wu, and J.C. Grossman (2010) doi:10.1103/PhysRevLett.104.016602.
5. G. Mahan, S. Brian, and J. Sharp (1997) doi:10.1063/1.881752.
6. R. Venkatasubramanian, E. Siivola, T. Colpitts, and B. O'Quinn (2001) doi:10.1038/35098012.
7. J. Walachová, R. Zeipl, J. Zelinka, and V. Malina (2005) doi: 10.1063/1.2001755.
8. J.M. Zide, D.O. Klenov, S. Stemmer, A.C. Gossard, G. Zeng, J.E. Bowers, D. Vashaee, and A. Shakouri (2005) doi: 10.1063/1.2043241.
9. H. Lu, P.G. Burke, A.C. Gossard, G. Zeng, A. T. Ramu, J.-H. Bahk, and J.E. Bowers (2011) doi:10.1002/adma.201100449.
10. W. Kim, J.M.O. Zide, A.C. Gossard, D.O. Klenov, S. Stemmer, A. Shakouri, and A. Majumdar (2006) doi: 10.1103/PhysRevLett.96.045901.
11. W. Kim, S.L. Singer, A. Majumdar, J.M.O. Zide, D. Klenov, A.C. Gossard, and S. Stemmer (2008) doi:10.1021/nl080189t.
12. W. Kim and A. Majumdar (2006) doi:10.1063/1.2188251.
13. D.G. Cahill, K. Goodson, and A. Majumdar (2002) doi: 10.1115/1.1454111.
14. D.G. Cahill, W.K. Ford, K.E. Goodson, G.D. Mahan, A. Majumdar, H.J. Maris, R. Merlin, and S.R. Phillpot (2003) doi:10.1063/1.1524305.
15. D.C. Driscoll, M. Hanson, C. Kadow, and A.C. Gossard (2001) doi:10.1063/1.1355988.
16. A. Guivarch, Y. Ballini, Y. Toudic, M. Minier, P. Auvray, B. Guenais, J. Caulet, B. Le Merdy, B. Lambert, and A. Regreny (1994) doi:10.1063/1.356181.
17. M.P. Hanson, D.C. Driscoll, C. Kadow, and A.C. Gossard (2004) doi:10.1063/1.1639932.

18. C.J. Palmstrom, *Annu. Rev. Mater. Sci.* 25, 389 (1995).
19. B.E. Warren, *X-ray Diffraction* (New York: Dover, 1969), pp. 29–41.
20. D.T. Cromer and J.B. Mann (1968) doi:10.1107/S0567739468000550.
21. K. Hiramatsu, S. Itoh, H. Amano, I. Akasaki, N. Kuwano, T. Shiraishi, and K. Oki, Growth mechanism of GaN growth on sapphire with AlN buffer layer by MOCVD. *J. Cryst. Growth* 115, 628 (1991).
22. T.E. Buehl, C.J. Palmstrøm, and A.C. Gossard (2011) doi:10.1116/1.3549888.
23. Y.K. Koh, S.L. Singer, W. Kim, J.M.O. Zide, H. Lu, D.G. Cahill, A. Majumdar, and A.C. Gossard (2009) doi:10.1063/1.3078808.
24. S. Adachi (2007) doi:10.1063/1.2779259.
25. J. Feser, Scalable Routes to Efficient Thermoelectric Materials, Ph.D., University of California, Berkeley, April 2011, 110 p; AAT 3444631.